The Two Lines Light Source (TLLS)

Wook Yeon Hwang Gabriel Taubin
Brown University
{wookyeon_hwang,taubin}@brown.edu

Abstract

Several 3D imaging methods based on active illumination, such as silhouette-based 3D reconstruction and structured light 3D scanning with binary patterns, require light sources capable of generating shadows with sharp boundaries when they are used to illuminate opaque occluders. Supported by empirical evidence suggesting that a low cost Uncollimated Laser Diode (ULD) produces shadows with sharp boundaries not requiring focusing in a wide range of depths, this paper proposes the use of ULDs as light sources in the target applications. Since due to astigmatism the Point Light Source (PLS) is not an accurate mathematical model of light propagation for the ULD, the Two Lines Light Source (TLLS) model is introduced to explain the observed behavior of the ULD. This novel geometric model of light propagation is defined by two 3D line segments, rather than a single 3D point, and guarantees that for each illuminated 3D point there exists a unique ray, which simultaneously passes through the point and intersects the two line segments. Furthermore, the equation of this ray can be computed in closed form at very low computational cost, and the TLLS model reduces to the PLS model when the two line segments intersect. Finally, the paper introduces a calibration method to estimate the model parameters, and describes the experiments performed to validate the model.

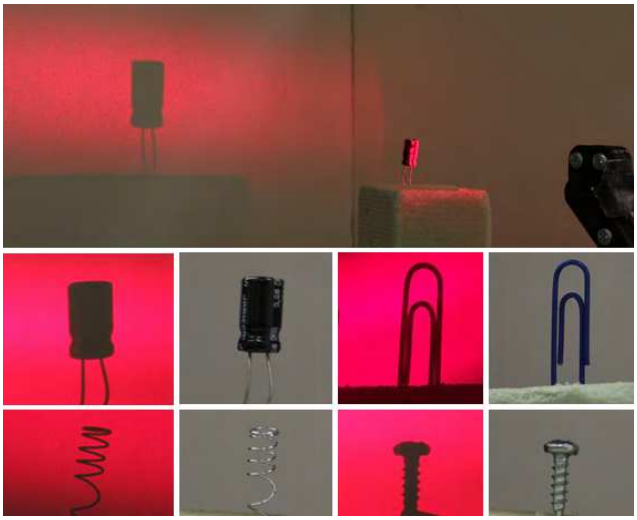

Figure 1. Preliminary experiments show that when an opaque occluder is illuminated by an uncollimated laser diode, magnified shadows with sharp edges are produced on a screen placed at a wide range of distances behind the occluder.

1. Introduction

An optical comparator is a device that applies the principles of optics to the inspection of manufactured parts. In an optical comparator, the magnified silhouette of a part is projected upon a screen, and the dimensions and geometry of the part are measured against prescribed limits. The optical comparator was invented by James Hartness in 1922 [15], in particular to address the problem of inspecting screw threads. Optical comparators have been used in machine shops since then, and have not changed very much in design over the years. To obtain accurate measurements with this instrument the object or feature being observed must be compared to a standard of known size. The first application of this principle was called a shadowgraph. This instrument used a lamp to project a two dimensional image of the object being observed on a flat surface. The shadow could then be measured with a known standard, such as a ruler, to determine its size. This type of comparison allowed an inspector to determine if a part was in or out of tolerance. Modern optical comparators comprise imaging sensors so that the comparisons are made using image processing software. Accurate measurements require shadows with sharp boundaries, as well as mathematical models of light propagation and shadow formation to relate the shadow boundaries to the 3D dimensions of the inspected part. Figure 2 shows a typical optical comparator, and a schematic drawing of a modern optical comparator design [13]. The mathematical models underlying 3D imaging algorithms based on active illumination, such as Shape-from-Silhouette (SfS) 3D reconstruction [2, 1, 8, 17, 9], and structured light 3D scanning based on projecting binary patterns [14], are also based on the assumption that the light sources are capable

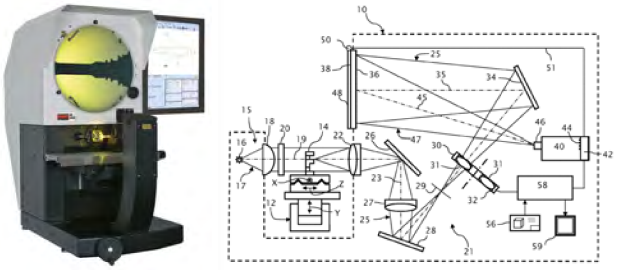

Figure 2. An industrial optical comparator, and a typical design of a modern optical comparator [13].

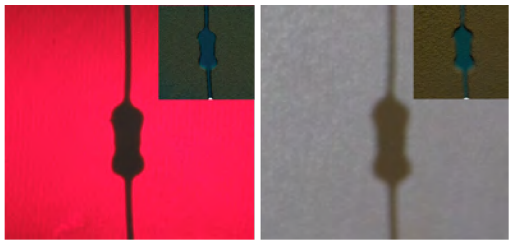

Figure 3. Silhouette shadows of a small resistor projected on a screen using an ULD compared with those resulting from using a LED.

of generating shadows with sharp boundaries when they are used to illuminate opaque occluders.

2. Light Sources

In SfS 3D reconstruction, using a small Extended Light Source (ELS) such as a high intensity LED results in blurred shadow boundaries. Figure 3 shows an example where shadows are produced using both an ULD and an LED to illuminate the same small object, under similar conditions (distance from light source to object, and from object to screen). In structured light 3D scanning, using a lens to focus a binary pattern on an object is intrinsically flawed due to depth of field constraints, because out of focus binary patterns look like shadow with blurred boundaries as well. Diffraction Optical Elements (DOE) [3], which do not require focusing with lenses, are used in certain single-shot 3D scanning devices, such as the Microsoft Kinect V1 [12], but the technology is not appropriate to develop high resolution 3D scanners. In theory, using a Point Light Source (PLS) without focusing lenses to illuminate the occluders would solve the problems in the two applications mentioned above, but unfortunately the PLS is a theoretical concept which does not exist in the physical world. In most typical applications, the dimensions of the light emitting surface of the ELS are not insignificant with respect to the dimensions of the overall imaging apparatus, and in particular with respect to the dimensions of the object, resulting in shadows with blurred boundaries. Furthermore, modeling the image formation process using extended light sources results in complex equations which are usually impossible to solve in practice.

3. The Uncollimated Laser Diode

Figure 1 contains results of some preliminary experiments which show that a low cost Uncollimated Laser Diode (ULD) produces shadows with sharp boundaries when it is used to illuminate an opaque occluder without any additional optical components, and the sharp boundaries are maintained within a wide range of depths. It is well known that an ULD is a light source that produces divergent rays, but the property illustrated in Figure 1 has neither been documented in the optics literature nor in the computer vision literature. This discovery has led us to believe that ULDs could be used as light sources in the target 3D imaging and metrology applications, potentially resulting in low cost precise industrial inspection, metrology, and 3D imaging systems. The main goal of this paper is to develop the mathematical foundations to enable these applications. Most light beams generated by semiconductor lasers are characterized by ellipticity, astigmatism, and large divergence. These properties are undesirable for light beam generation and are usually optically corrected. Due to diffraction, the beam diverges (expands) rapidly after leaving the chip, typically at 30 degrees vertically by 10 degrees laterally. Also, as a consequence of the rectangular shaped active layer and the non-uniform gain profile within the active layer, laser diode beams are astigmatic. Astigmatism is a well known and documented property of laser diodes [16] and even standards exist to measure it [4]. An astigmatic laser beam does not emerge from a single 3D point, but appears to be emerging from multiple locations. As a result of astigmatism the PLS model turns out not to be an accurate geometric model of light propagation for the ULD. Since astigmatism can vary from one laser diode to another even of the same type, calibration procedures are required to guarantee precise measurements. This paper introduces the Two Lines Light Source (TLLS) model as a novel geometric model of light propagation, which accurately describes the observed behavior of ULDs. We found close similarity of geometrical representation between crossed-slit camera and TLLS model[18, 11]. However, we would like to emphasize that the reason we introduced the two-line model is that when utilizing uncollimated laser propagation as a light source, it is essential to estimate the astigmatism of the laser for the calibration procedure in 3D application. The TLLS model has a simple and elegant formulation defined by two 3D line segments, rather than the single 3D point which defines the PLS model, but it reduces to the PLS model when the two segments intersect. As a result, the TLLS model is a natural generalization of the PLS model. As in the PLS model, for each illuminated 3D point there exists a unique ray emitted by the light source passing through the point,

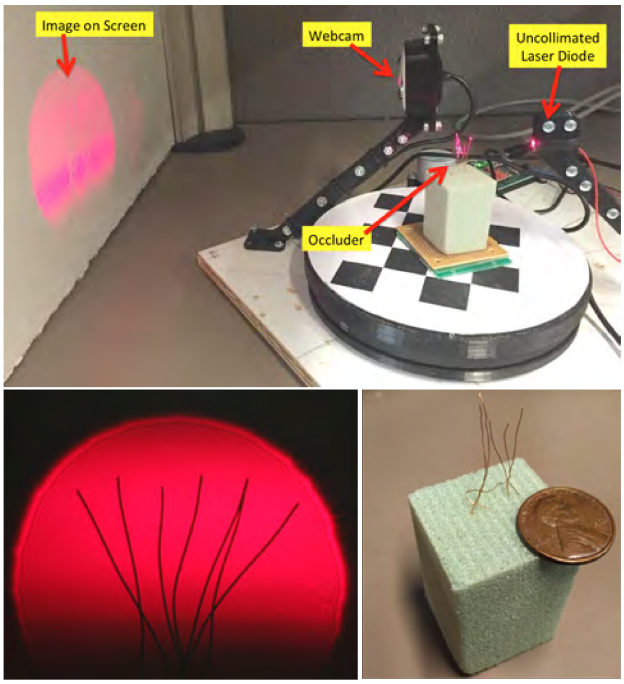

Figure 4. Experimental setup for preliminary experiments which lead to the TLLS model.

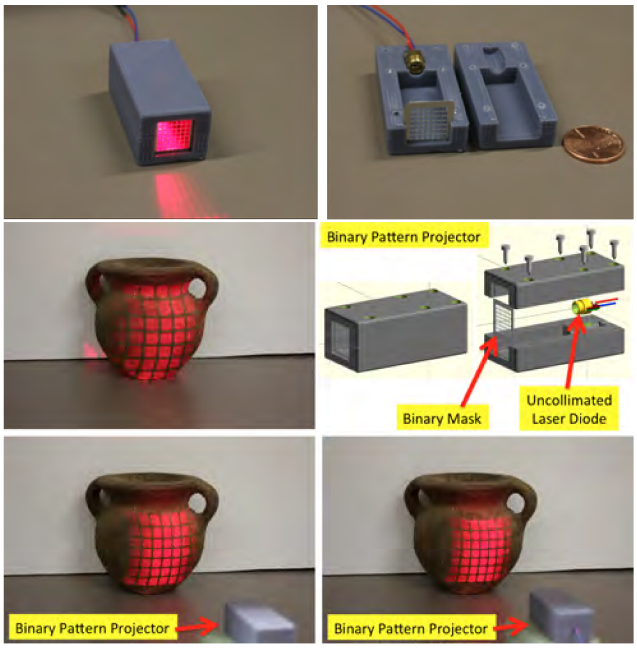

Figure 5. A simple 3D printed pattern projector constructed using a ULD and a metal mask projects focus-free binary images on a 3D scene within a wide range of depths.

which can be described in closed form, and can be estimated in constant time at low computational cost. Finally, the paper introduces a calibration method to estimate the model parameters, and describes the experiments performed to validate the model. Figure 4 shows the experimental setup and results of early experiments which lead to the formulation of the TLLS model. The wires are illuminated by an ULD. An image is formed on a white screen, where the wires cast shadows with very sharp boundaries. Using a different extended light source, such as a high intensity white LED, the shadows are blurred, and the silhouettes of the wires on the screen cannot be determined precisely. Figure 5 illustrates a preliminary attempt at constructing focus free binary pattern projectors, eventually to be used in structured light 3D scanning applications. A thin metal mask is illuminated by a low cost uncollimated laser diode, which resulted from removing the collimating lens from a laser beam module such as those used in laser pointers. An enclosure was 3D printed to mount the laser diode at a fixed distance from the mask, and to prevent spurious emission of light, other than through the mask. The figure shows a rendering of a CAD model of the prototype device, as well as three images of a clay pot illuminated by this pattern projector with the distance between the projector and the object varying in a range larger than the size of the object. The pattern projector can be seen at the bottom of two of these images. Because of the divergent rays, the projected pattern varies in size as a function of the distance from the projector to the object, what is most important to observe here is that the projected binary pattern is in focus in all cases. In this paper we are not exploring any of the applications listed in the introduction, but we plan to do so in the near future.

4. Modeling Extended Light Sources

To simplify the analysis we will model the light emitting surface of the laser diode as a small rectangle contained in the plane $z = 0$ aligned with the x and y Cartesian axes, centered at the origin, and with the light emitted only in the direction of $z > 0$. A function $I(x, y, v)$ which attains non-negative values measuring the directional light intensity emitted in the direction of the unit length vector v so that $v_z > 0$ from the point (x, y) within the light emitter rectangle can be used as a general mathematical model to describe the rectangle as an extended light source where each point on the light emitter surface has a different directional distribution. We have decided not to include phase information in this model, despite the fact that a laser diode emits coherent light. Section 12 includes a discussion of diffraction effects and plans for related future work where phase information will be incorporated into the model. In fact this representation corresponds to a file format which has been standardized [6] to contain the information represented by the function $I(x, y, v)$, as well as additional information. The so called *Ray Files* are predefined ray tables consisting of xyz starting points and direction vectors, as well as polarization states, wavelength data, and the initial flux value or Stokes Vector for each ray. Ray files are typ-

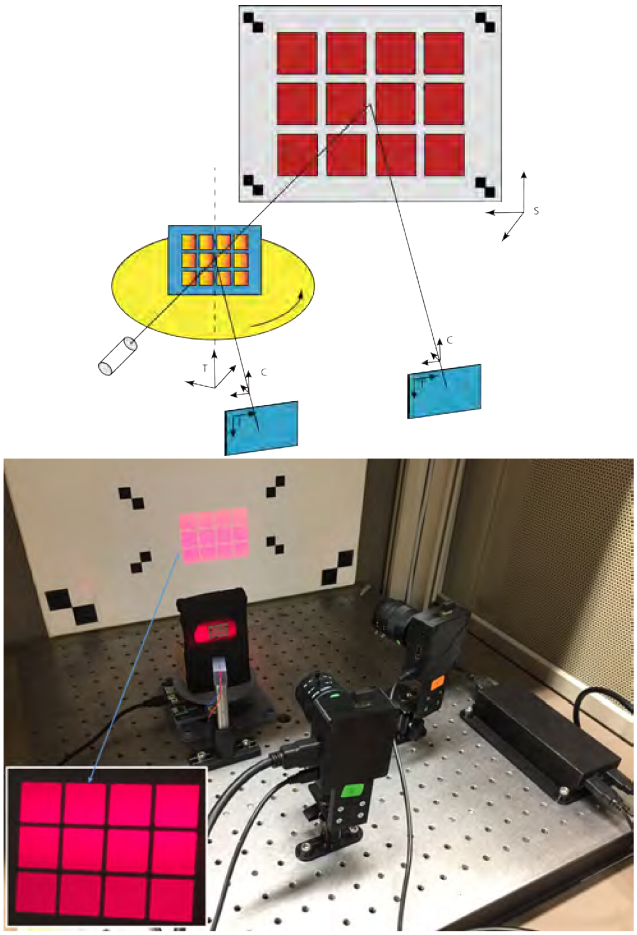

Figure 6. Experimental setup used to sample the rays emitted by an ULD and to estimate the parameters of the TLLS model, using binary masks of known dimensions as occluders.

ically created from measured results or theoretical calculation and are used in illumination design software.

5. Directional Extended Light Sources

The model $I(x, y, v)$ introduced in the previous section can be regarded as a Light Field [10] with the light traversing the rays in the opposite direction, and it is too general to describe the behavior of the ULD. To explain the sharp shadow boundaries it is necessary that for each point (x, y) in the light emitting surface the function $I(x, y, v)$ be close to zero except for a small region concentrated around a particular unit length direction vector $v(x, y)$ which could change from point to point. In the limit case the function $I(x, y, v)$ would be a generalized function

$$I(x, y, v) = I(x, y)\, \delta(v - v(x, y)) \qquad (1)$$

where $I(x, y)$ is a non-negative scalar function, and $\delta(\cdot)$ is Dirac's delta function. That is, the function $I(x, y, v)$ is zero everywhere, except for $v = v(x, y)$, where it attains the

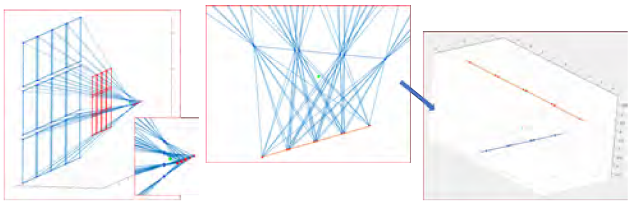

Figure 7. Visualization of vector light field sampling results corresponding to the experimental setup of figure 6

value $v(x, y)$. Note that the ideal point light source satisfies this model, where $v(x, y)$ is the vector going from the point source to the point $(x, y, 0)$, normalized to unit length. We will refer to this model as the Directional Extended Light Source(DELS) model, and to the vector function $v(x, y)$ as the Vector Light Field of the model.

6. Sampling The Vector Light Field

The ULD satisfies the properties which define the DELS model, but the DELS model is still far to general. The next step is to determine a proper family of vector light fields to represent ULDs. This family should ideally have a parametric form defined by a few parameters. Since no such model has been disclosed in the literature, we designed an experimental setup to sample the vector light field, so that we could visualize the corresponding rays inside the laser diode. Figure 6 shows the experimental setup. In the bottom photo, a shutter-less camera, shown in the middle, is used in these experiments to capture images of test grid pattern. The additional shutter-less camera, shown on the right hand side of the photo, is used to capture the shadow image formed on the screen. The inset photo is just a picture of the shadow projected on the screen with sharp boundaries. First of all, the intrinsic parameters of the camera are calibrated using standard techniques, and the camera coordinate system is used as the global coordinate system. A thin chemically etched metal mask comprising an array of 3×4 square holes is used as the occluder, because of its similarity to a checkerboard. The corners of mask are detected in the image using a modified checkerboard detection algorithm: the boundary edges of the mask squares are detected and segmented into collinear groups; a straight line is fit to each group; the pixel locations of the square corners are estimated as the intersections of vertical and horizontal lines. Since the mask dimensions are known, the pose of the mask in the global coordinate system is determined as a function of the pixel coordinates of the labeled square corners using a well know checkerboard pose estimation algorithm. The screen is fabricated with a few markers which are used to determine the implicit equation of the plane. With minimal modifications, the same algorithm used to detect the corners of the mask is used to detect the corners of the square from the shadow projected on the screen. The pixel coordinates

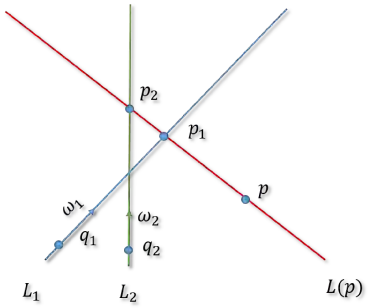

Figure 8. The Two Lines Light Source model is defined by the two lines L_1 and L_2. For each point p in 3D, which does not belong to the two planes parallel to the two lines containing one of the lines, there exists a unique line L which contains p and intersects L_1 and L_2.

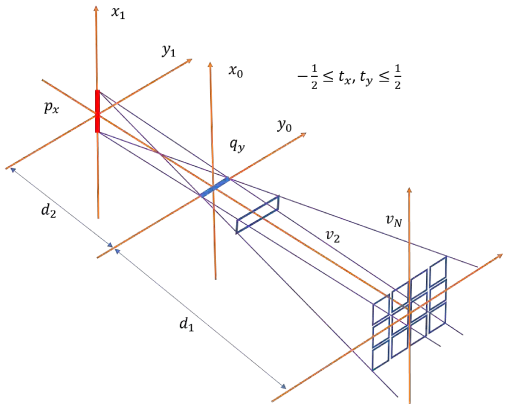

Figure 9. The Two Lines Light Source model typical geometric configuration for an ideal ULD, showing the emitter rectangular window, and the mask used in the sampling experiments.

of each of these corners defines a ray which passes through the corresponding screen point and the center of projection of the camera. The intersection if this ray, represented in parametric form, with the screen plane, represented in implicit form, yields the 3D coordinates of the corresponding square corner in the screen. For each of the 48 square corners of the mask we now have its 3D coordinates, as well as the 3D coordinates of a corresponding screen point. These two points belong to the same ray emitted by the laser, and are used to determine the equation of the straight line supporting the ray. We can now visualize these 48 straight lines and draw some conclusions. Figure 7 shows a visualization of these lines. It is quite clear that they do not converge on a single 3D point. As a result, although the ULD emits rays which diverge and do not seem to intersect within the working volume, it does not behave like a PLS. However, we do observe a much more interesting, and quite unexpected, phenomenon. In fact, we consider this discovery one of the main contributions of this paper. The 6 rays corresponding to the square corners which belong to each vertical straight line of the mask grid seem to intersect on a common point, and these 8 common points seem to be collinear. At the same time, the 8 rays corresponding to the square corners which belong to each horizontal straight line of the mask grid seem to intersect on a common point as well, and these 6 common points seem to be collinear as well. The two straight lines joining the vertical and horizontal common points are different; in fact they do not seem to intersect, and they seem to be orthogonal. In particular, each of the estimated rays intersects the two common lines.

7. The Two Lines Light Source

Based on the results of the experiments described in the previous section, we propose the Two Lines Light Source (TLLS) model. The model is defined by two straight lines L_1 and L_2 which we prefer to describe in parametric form as $L_1 = \{q = q_1 + t_1\, w_1\}$ and $L_2 = \{q = q_2 + t_2\, w_2\}$, where q_1 and q_2 are 3D points, w_1 and w_2 are two linearly independent unit length vectors, and t_1 and t_2 are scalar parameters. Of course, the points q_1 and q_2 are not uniquely determined, since if they are replaced by other points which belong to the same straight line, the line does not change. In practice the scalar parameters t_1 and t_2 are bound above and below by certain values, but we prefer not to introduce those parameters at this point. In the case of the ULD, the light emitting surface can be regarded as a rectangular aperture so that only rays that cross the aperture are light carrying. If the axes of the rectangular aperture are parallel to the vectors w_1 and w_2, then the aperture determine natural bounds on t_1 and t_2. Let us consider the two parallel planes spanned by the vectors w_1 and w_2; the first one containing the line L_1, and the second one containing the line L_2. The main property of this model is that for each 3D point p which does not belong to either one of these two planes, there exist a unique line $L(p)$ which intersects both lines. To determine the equation of this line, we observe that since the point p does not belong to the line L_1, there exists a unique plane π_1 which contains the line L_1 and the point p; and similarly, since the point p does not belong to the line L_2, there exists a unique plane π_2 which contains the line L_2 and the point p. These two planes are different because the lines L_1 and L_2 are not parallel. The plane π_1 can be described in implicit form as $\pi_1 = \{q : n_1^t(q - q_1) = 0\}$, where $n_1 = w_1 \times (p - q_1)$. Similarly the plane π_2 can be described in implicit form as $\pi_2 = \{q : n_2^t(q - q_2) = 0\}$, where $n_2 = w_2 \times (p - q_2)$. It is not difficult to verify that for every point p not belonging to the two excluded planes, the plane π_1 and the line L_2 intersect in a single point q_2, and the plane π_2 and the line L_1 intersect in a single point q_1. For the points p in the excluded planes, one of the two intersections may not occur because of parallelism. Finally, since the points p, q_1, and q_2 simultaneously belong to the

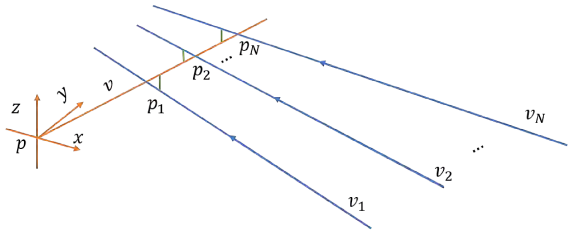

Figure 10. Geometric construction used to define the refinement procedure.

planes π_1 and π_2, they are collinear. The straight line $L(p)$ is the intersection of the planes π_1 and π_2, and can be defined in parametric form as $L(p) = \{q = q_1 + \lambda\,(q_2 - q_1)\}$, where λ is a scalar parameter. Figure 9 show the geometric configuration which appear to apply to the experimental setup described above. There is neither guarantee that the two lines will be perpendicular to each other, nor that they will be aligned with the Cartesian axes. The next section describes a calibration procedure to determine the actual parameters. But if the point p is a point belonging the the emitting window $p = (x, y, 0)^t$, the vector $v(x, y)$ is the result of normalizing the vector $q_2 - q_1$ to unit length, and if necessary invert its orientation so that $v_z > 0$.

8. Calibration

The purpose of the calibration procedure is to estimate the parameters of the TLLS model introduced in the previous section, namely the parametric equations of the lines L_1 and L_2, in the camera coordinate system, which is regarded as the world coordinate system. But before attempting to do so, the camera intrinsic parameters should be calibrated, and the pose of of the screen plane with respect to the camera has to be determined. Since our calibration procedure uses two cameras, both cameras need intrinsic calibration and the relative position and orientation of the second camera looking at the mask has to be estimated as well. In particular, after calibrate intrinsic parameters for both camera focusing at the imaging screen, we compute extrinsic parameters of the first camera and find the relative position of the second camera with respect to the first camera. Then recalibrate intrinsic parameters of the second camera focusing at the calibrate pattern on the turn-table. Instead of using a separate checkerboard placed in different positions and orientations within the field of view of the camera, we use the metal mask pattern object and its projected images (minimum 3 images with different locations of pattern) detected. Since the scanning system comprises a rotational turntable, we use the turntable to move the metal mask within the camera calibration phase, capture images of the metal mask, and use the detected corners of the squares as inputs to the routines which estimate the intrinsic parameters.

Then we follow the same procedure described above to capture images of the metal mask and their shadows on the screen, and detect the pairs of corresponding corners. In fact, we can use the same images to calibrate the camera, and then to perform this step. We detect $N = 48$ pairs of corners in each image, which result in 48 measured rays. Let $p_1^M, \ldots, p_N^M$ be the 3D coordinates of the corners detected in the mask, and $p_1^S, \ldots, p_N^S$ the 3D coordinates of the corresponding corners detected on the screen. The next section describes the procedure that we implemented to obtain initial estimates for the TLLS model parameters. Let's assume here that we already have these initial estimates. Based on these parameters we can determine the equations of the unique line $L(p_k^M)$ passing through the point p_k^M predicted by the model. Let π_S denote the screen plane. The intersection of the line $L(p_k^M)$ and the plane π_S is a point q_k^S, which is likely to be different from the point p_k^S. We propose as the calibration procedure the global minimization of the following *bundle adjustment* objective function, which somehow measures the sum of the squares of the divergence between corresponding measured and predicted rays.

$$E(L_1, L_2) = \sum_{k=1}^{N} \|q_k^S - p_k^S\|^2 \tag{2}$$

Since this is a non-linear multimodal objective function, our approach is to identify an approximate solution by solving the related optimization problem decribed in Section 9, for which an analytic solution exists, and then refine the approximate solution by locally minimizing the non-linar least squares bundle adjustment objective function using the Levenberg-Marquardt algorithm as described in Section.10.

9. Initial Estimates using Plücker Coordinates

A straight line in 3D can be represented by a 2×4 matrix defined by a pair of points which belong to the line

$$\begin{bmatrix} p_x & p_y & p_z & 1 \\ q_x & q_y & q_z & 1 \end{bmatrix} \tag{3}$$

This representation is, of course, not unique. The Plücker coordinate of this line can be defined as the 6-dimensional vector X whose coordinates are

$$\begin{aligned} X_{12} &= p_x q_y - q_x p_y \\ X_{13} &= p_x q_z - q_x p_z \\ X_{14} &= p_x - q_x \\ X_{23} &= p_y q_z - q_y p_z \\ X_{24} &= p_z - q_z \\ X_{34} &= q_y - p_y \end{aligned} \tag{4}$$

Given two 2×4 matrix representations of the same straight line, their corresponding Plücker coordinates are the same except for a multiplicative constant. That is, the mapping

which computes the Plücker coordinates produces a point in P^5. Not every point in P^5 is the Plücker coordinate of a straight line in 3D though. Actually the image of the Plücker map forms a quadric Q in P^5 defined by the zeros of the polynomial

$$f(X) = X_{12}X_{34} - X_{13}X_{24} + X_{14}X_{23} \tag{5}$$

Given four straight lines in general position in 3D, it is a clasical result that there exists exactly two other straight lines that intersect the given four [5]. A simple algorithm to determine these two lines, along with the mathematical foundations of the method, are described in detailed for example in [7]. It comprises the following steps: 1) constructing a 6×4 matrix by concatenating the Plücker coordinates vectors of the four given lines as columns; 2) determining a basis of the two dimensional subspace orthogonal to the four dimensional subspace spanned by the four vectors of Plücker coordinates (numerically, this can be achieved by computing the singular value decomposition of the 6×4 matrix, and determining the two singular vectors corresponding to the two zero singular values); 3) this two dimensional subspace is actually a straight line in P^5 which intersects the quadric Q in two points; determine the two intersection points; 4) these two points in P^5 are guaranteed to be the Plücker coordinates of two different straight lines in 3D; determine those two lines. Given N straight lines, such as the measured rays used as the calibration data, the previous SVD-based algorithm can be generalized, replacing the 6×4 matrix by the $6 \times N$ matrix resulting from concatenating the Plücker coordinates of the N straight lines, and determining the two dimensional subspace spanned by the two left singular vectors associated with the two smallest singular values.

10. Fine Search for two lines

In the previous section we introduced a method to determine initial estimates of the two lines minimizing the objective function of equation 2. We have determined in practice that these initial estimates are often not good enough, and a descent procedure is required to refine these estimates. The input data to both the initialization procedure and the refinement procedure are the points $p_1^M, \ldots, p_N^M$ detected on the mask, and the points $p_1^S, \ldots, p_N^S$ detected on the screen, which define the ray samples obtained from measurements. To simplify the notation in this section, let's replace p_k^M by p_k, and let v_k ne the result of normalizing the vector $p_k^M - p_k^S$ to unit length. Each pair (p_k, v_k) defines the parametric equation of a line supporting a measured ray. Since the two straight lines L_1 and L_2 that define the TLLS model should intersect the N measured lines, our approach here is to look at the function which measures the sum of the square distances from an arbitrary line to the N measured lines, and search the domain of this function with the expectation that two different local minima could be identified. Let $L_h = \{p = p_h + t_h\, v_h\}$ be a straight line described in parametric form, where p_h is a 3D point, v_h is a unit length 3D vector, and t_h is a scalar parameter. Let $L_j = \{p = p_j + t_j\, v_j\}$ be another straight line described in parametric form. Furthermore, let's assume that the two lines are neither parallel nor intersect, which is equivalent to requiring that the three vectors v_h, v_j, and $p_j - p_h$ be linearly independent. It is well known that the following equation describes the square of the distance between the two lines

$$dist(L_h, L_j) = \left(\frac{(v_h \times v_j)^t (p_h - p_j)}{\| v_h \times v_j \|} \right)^2 \tag{6}$$

It follows that given N lines $L_1, \ldots, L_N$ defined in parametric form $L_k = \{p = p_k + t_k\, v_k\}$, the following expression describes the average square distance from an additional line $L = \{p = p + t\, v\}$ also defined in parametric form to the N given lines

$$E(L) = \frac{1}{N} \sum_{k=1}^{N} \left(\frac{(v \times v_k)^t (p - p_k)}{\| v \times v_k \|} \right)^2 \tag{7}$$

which can also be written as follows

$$E(L) = \frac{1}{N} \sum_{k=1}^{N} \left(w_k^t (p - p_k) \right)^2 \tag{8}$$

where $w_k = (v \times v_k) / \| v \times v_k \|$. Note that for fixed values of $v, v_1, \ldots, v_N, p_1, \ldots, p_N$ the objective function $E(L)$ is a quadratic non-negative function of p. This expression measures the average square distance from the line parallel to the vector v, which minimizes the average square distance to the given lines $L_1, \ldots, L_N$. By performing this procedure, after the initial estimation method described in the previous section, we can refine the estimates of the two line parameters.

11. Results

The two images on the right hand side of Figure 11 show the result of the calibration procedure described above in the form of reprojection error in a 3D view and on the screen. The two images on the left hand side show similar results but using a PLS model fitted to the measured rays. We have a mean error value of approximately 0.1% with TLLS while PLS gives 0.9%. As we can see in Figure 11(left), the reprojected grid pattern drawn by blue is not well coincide with projected pattern image in the screen. We have computed the two line model from multiple positions and orientation of test grid pattern as shown in Figure 12. This step will verify whether the same two line model can be

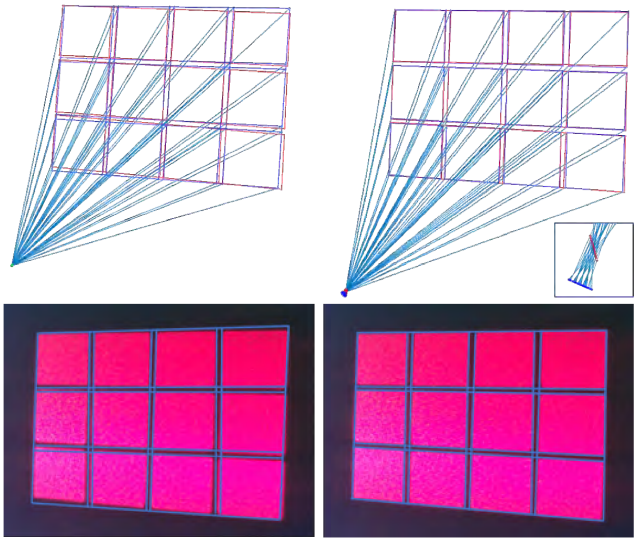

Figure 11. Reprojection from PLS model(left) and Reprojection from TLLS model(right)

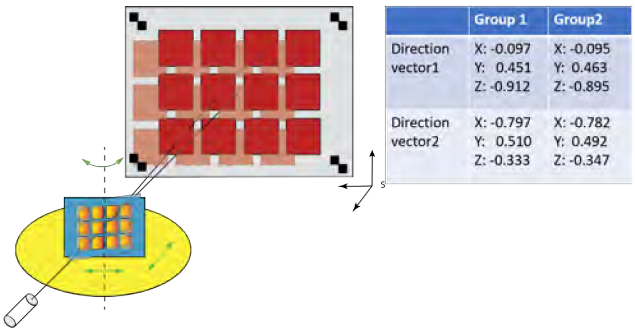

Figure 12. A geometric configuration for multiple measurements.

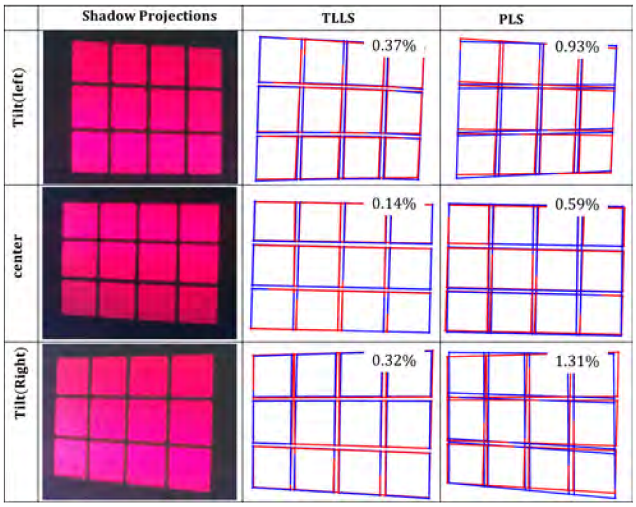

Figure 13. Comparison of results for different orientation of the test pattern. The captured pattern is drawn in red and the estimation from each method is drawn in blue. The mean error is normalized by the diagonal distance of the pattern image in the screen.

Figure 14. Diffraction will have to be considered in future work.

found when the location of the test pattern is changed with stationary camera and imaging screen. We compared two groups, each calculated from 10 different locations of the test pattern. As shown in Figure 12, the direction vectors for two lines from two groups are similar and the two-line parameters obtained from multiple images with different locations of the test patterns give similar reprojection errors of 0.17%. We also conducted experiment with 3 different orientation of the test grid pattern to compare TLLS and PLS case. As shown in Figure 13, we have better mean error with TLLS in every case. The discrepancy of error between the two cases is increasing when angle increases between the pattern and the center propagation of the laser. These additional experiments showed that our assumption of TLLS is plausible and ULD is non-central light source thus, the points light source is not a good approximation.

12. Conclusions and Future Work

The main contribution of the paper is the development and formulation of the TLLS model, based on the unexpected properties of the ULD. In future work, we will explore the application of this technology in 3D shape capture systems. Figure 14 shows an experiment where an ULD was used to illuminate a straight edge mask occluder, and the shadow was produced onto a toy football. The distance between the occluder and the object is the same in both images, but the distance between the ULD and the occluder is larger in the left image compared to the right image. In this example the left image, where the ULD is far away from the occluder, shows shadows with sharp boundary, but the effect of diffraction is evident in the right image, where the ULD is much closer to the occluder. This experiment shows that in practice the effect of diffraction can be minimized by adjusting the distances between ULD, occluder, and object, and justifies our decision of not incorporating phase information in the TLLS model introduced in this paper. However, an extended TLLS model which incorporates phase information is needed at least to accurately predict the effect of diffraction. We plan to develop such extended model in the near future.

References

[1] N. Ahuja and J. Veenstra. Generating Octrees from Object Silhouettes in Orthographic Views. *IEEE Transactions on Pattern Analysis and Machine Intelligence*, 11(2):137–149, Feb. 1989. doi:10.1109/34.16710. 4321

[2] B. Baumgart. *Geometric Modeling for Computer Vision*. PhD thesis, Stanford University, 1974. 4321

[3] Holoeye diffractive optical elements. http://holoeye.com/diffractive-optics/. 4322

[4] Iso 11146-1:2005, lasers and laser-related equipment – test methods for laser beam widths, divergence angles and beam propagation ratios – part 1: Stigmatic and simple astigmatic beams. International Organization for Standarization, Jan. 2005. https://www.iso.org/standard/33625.html. 4322

[5] S. L. Kleiman and D. Laksov. Schubert calculus. *The American Mathematical Monthly*, 79(10):1061–1082, 1972. 4327

[6] J. Koshel, I. Ashdown, W. Brandenburg, D. Chabaud, O. Dross, S. Gangadhara, K. Garcia, M. Gauvin, G. Gregory, D. Hansen, K. Haraguchi, G. Hansa, J. Jiao, R. Kelley, and J. Muschaweck. Data Format for Ray File Standard. In *Proceedings of Renewable Energy and the Environment, Freeform Optics*, Tucson, Arizona, United States, Nov. 2013. Optical Society of America. 4323

[7] D. Lanman, M. Wachs, G. Taubin, and F. Cukierman. Reconstructing a 3d line from a single catadioptric image. In *3D Data Processing, Visualization, and Transmission, Third International Symposium on*, pages 89–96. IEEE, 2006. 4327

[8] A. Laurentini. The Visual Hull: A New Tool For Contour-Based Image Understanding. In *Proceedings of the 7th Scandinavian Conference on Image Analysis*. Pattern Recognition Society of Denmark, 1991. 4321

[9] A. Laurentini. The Visual Hull Concept for Silhouette-Based Image Understanding. *IEEE Transactions on Pattern Analysis and Machine Intelligence*, 16(2):150–162, Feb. 1994. doi:10.1109/34.273735. 4321

[10] M. Levoy and P. Hanrahan. Light Field Rendering. In *Proceedings of the 23rd Annual Conference on Computer Graphics and Interactive Techniques (Siggraph'96)*, pages 31–42, 1996. doi:10.1145/237170.237199. 4324

[11] N. Li, H. Lin, B. Sun, M. Zhou, and J. Yu. Rotational crossed-slit light field. In *Proceedings of the IEEE Conference on Computer Vision and Pattern Recognition*, pages 4405–4413, 2016. 4322

[12] Microsoft. Kinect for Xbox 360. http://en.wikipedia.org/wiki/Kinect, nov 2010. 4322

[13] E. Polidor. Method of Inspecting Test Parts With an Optical Comparator Having Digital Gage. US Patent No. 8,400,633 B2, Mar. 2013. 4321, 4322

[14] J. Salvi, J. Pags, and J. Batlle. Pattern Codification Strategies in Structured Light Systems. *Pattern Recognition*, 37(4):827–849, Apr. 2004. doi:10.1016/j.patcog.2003.10.002. 4321

[15] K. Smith. Shedding Light on Optical Comparators. *Quality Digest*, May 2002. http://www.qualitydigest.com/may02/html/optcomp.html. 4321

[16] H. Sun. Measurement of Laser Diode Astigmatism. *Optical Engineering*, 36(4):1082–1087, Apr. 1997. doi:10.1117/1.601147. 4322

[17] R. Szeliski. Rapid Octree Construction From Image Sequences. *CVGIP: Image Understanding*, 58(1):23–32, July 1993. doi:10.1006/ciun.1993.1029. 4321

[18] A. Zomet, D. Feldman, S. Peleg, and D. Weinshall. Mosaicing new views: The crossed-slits projection. *IEEE Transactions on Pattern Analysis and Machine Intelligence*, 25(6):741–754, 2003. 4322